

# Direction-sensitive dark matter search with the low-background gaseous detector NEWAGE-0.3b”

Tomonori Ikeda<sup>1,\*</sup>, Kiseki Nakamura<sup>1,2</sup>, Takuya Shimada<sup>1</sup>, Ryota Yakabe<sup>1</sup>, Takashi Hashimoto<sup>1</sup>, Hirohisa Ishiura<sup>1</sup>, Takuma Nakamura<sup>1</sup>, Hiroshi Ito<sup>2,3</sup>, Koichi Ichimura<sup>4</sup>, Ko Abe<sup>2,3</sup>, Kazuyoshi Kobayashi<sup>5</sup>, Toru Tanimori<sup>6</sup>, Hidetoshi Kubo<sup>6</sup>, Atsushi Takada<sup>6</sup>, Hiroyuki Sekiya<sup>2,3</sup>, Atsushi Takeda<sup>2,3</sup>, and Kentaro Miuchi<sup>1</sup>

<sup>1</sup>*Department of Physics, Graduate School of Science, Kobe University, Rokkodai-cho, Nada-ku, Kobe-shi, Hyogo, 657-8501, Japan*

<sup>2</sup>*Kamioka Observatory, Institute for Cosmic Ray Research, the University of Tokyo, Higashi-Mozumi, Kamioka-cho, Hida-shi, Gifu, 506-1205, Japan*

<sup>3</sup>*Kavli Institute for the Physics and Mathematics of the Universe (WPI), the University of Tokyo, 5-1-5 Kashiwanoha, Kashiwa-shi, Chiba, 277-8582, Japan*

<sup>4</sup>*Research Center for Neutrino Science, Tohoku University, Sendai 980-8578, Japan*

<sup>5</sup>*Waseda Research Institute for Science and Engineering, Waseda University, 3-4-1 Okubo, Shinjuku, Tokyo 169-8555, Japan*

<sup>6</sup>*Division of Physics and Astronomy, Graduate School of Science, Kyoto University, Kitashirakawa-iwake-cho, Sakyo-ku, Kyoto-shi, Kyoto, 606-8502, Japan*

\*E-mail: ikeda.tomonori.2s@kyoto-u.ac.jp

Received January 27, 2021; Revised April 9, 2021; Accepted April 22, 2021; Published April 29, 2021

NEWAGE is a direction-sensitive dark matter search using a low-pressure gaseous time projection chamber. A low alpha-ray emission rate micro pixel chamber had been developed in order to reduce background for dark matter search. We conducted the dark matter search at the Kamioka Observatory in 2018. The total live time was 107.6 d, corresponding to an exposure of 1.1 kg d. Two events remained in the energy region of 50–60 keV, which was consistent with the expected background of 2.5 events. A directional analysis was carried out and no significant forward–backward asymmetry derived from the WIMP-nucleus elastic scatterings was found. Thus a 90% confidence level upper limit on the spin-dependent WIMP-proton cross-section of 50 pb for a WIMP mass of 100 GeV  $c^{-2}$  was derived. This limit is the most stringent yet obtained from direction-sensitive dark matter search experiments.

Subject Index F41

## 1. Introduction

Dark matter is one of the biggest puzzles of modern cosmology and particle physics. A number of experimental efforts aiming to find the weakly interacting massive particle (WIMP) dark matter through direct searches which observe the scatterings of the WIMP and nuclei have been carried out [1–8]. However, the dark matter has not been discovered yet. In the direct search, the annual modulation and the directional signature would be two possible signals among the characteristic signals of the dark matter. The annual modulation is caused by the orbital motion of the Earth around the Sun. The modulation amplitude is expected to be a few per cent [9]. On the other hand, the directional signature is due to the circular motion of the solar system around the galaxy center. The forward–backward ratio in nuclear recoil angular distribution derived from the WIMP-nucleus elastic

scatterings could be an order of magnitude [10]. In addition, the directional method could discover the WIMP dark matter beyond the neutrino floor, which represents the ultimate background by the coherent neutrino–nucleus scatterings [11], and reveal the astrophysical and particle properties of the dark matter [12–14].

NEWAGE (NEW generation WIMP search with an Advanced Gaseous tracker Experiment) is a direction-sensitive WIMP dark matter search experiment using a low-pressure gas micro time projection chamber ( $\mu$ TPC) [15]. A direction-sensitive experiment needs to detect the direction of the recoil nuclei. Hence a TPC with low-pressure gas and a readout device,  $\mu$ -PIC [16], which is one variation of micro pattern gaseous detectors, are used. In 2015, an underground measurement was performed and the best directional constraint testing the forward–backward asymmetry in the nuclear recoil angular distribution was achieved [17]. We then increased the statistics by a factor of more than 10 and the first 3D-vector directional dark matter search was performed [18]. However, a certain amount of radioactivity, which potentially contributed to the background, was later found inside the  $\mu$ -PIC. Therefore the surface material of the  $\mu$ -PIC, which was the dominant background source, was replaced with less radioactive material. This newly developed low-background  $\mu$ -PIC was called a low alpha-ray emission rate micro pixel chamber (LA $\mu$ -PIC) [19]. In this paper, the first results of the direction-sensitive dark matter search using the LA $\mu$ -PIC are reported.

## 2. NEWAGE-0.3b” detector

The NEWAGE-0.3b’ detector was upgraded to NEWAGE-0.3b” by replacing the readout device from the standard  $\mu$ -PIC with the LA $\mu$ -PIC. Most of the detector system is unchanged and we briefly summarize the structure of the NEWAGE-0.3b” detector and its performance in this section.

### 2.1. System

The NEWAGE-0.3b” detector is a low-pressure gaseous  $\mu$ TPC that is composed of a LA $\mu$ -PIC [19], a gas electron multiplier (GEM [20]) and a TPC cage. The schematic drawing is shown in Fig. 1. The LA $\mu$ -PIC was manufactured by Dai Nippon Printing Co. Ltd. It has  $768 \times 768$  pixels with a pitch of  $400 \mu\text{m}$  forming the detection area of  $30.7 \times 30.7 \text{ cm}^2$ . These electrodes are connected by 768 anode strips and 768 cathode strips. The anode and cathode strips of LA $\mu$ -PIC are orthogonally formed and thus the 2D position of a hit pixel can be known. The structure of the pixel electrode is same as that of a standard  $\mu$ -PIC [16], while the material facing the detection volume was changed. Measurements of the U/Th contamination in the  $\mu$ -PIC components using a high-purity germanium detector indicated that the glass cloth-sheet has a large amount of radioactive contamination. Therefore, a compound of epoxy and polyimide without the glass cloth-sheet, which is a factor of 100 less contaminated by isotopes of  $^{238}\text{U}$  and  $^{232}\text{Th}$ , was chosen as a new surface material. Performance testing showed that the newly developed  $\mu$ -PIC works as the standard  $\mu$ -PIC does. Details can be found in Ref. [21]. A GEM with an effective area of  $32 \times 31 \text{ cm}^2$  is used as a first stage amplifier in order to obtain a sufficient gas gain while keeping a stable operation. The substrate of the GEM is a  $100\text{-}\mu\text{m}$ -thick liquid crystal polymer. Cylindrical holes are formed using the laser etching technique. The hole size and pitch are  $70 \mu\text{m}$  and  $140 \mu\text{m}$ , respectively [22]. The TPC field cage, which is made of four plates of polyether ether ketone plastic plates, was installed in order to make a uniform electric field. Copper wires with a spacing of 1 cm are placed on the side walls and chained by resistors. The TPC cage has a length of 41 cm. The vessel was filled with  $\text{CF}_4$  at 76 Torr.  $\text{CF}_4$  is chosen because of its small diffusion and a large cross-section for the spin-dependent (SD) interaction of fluorine. A gas

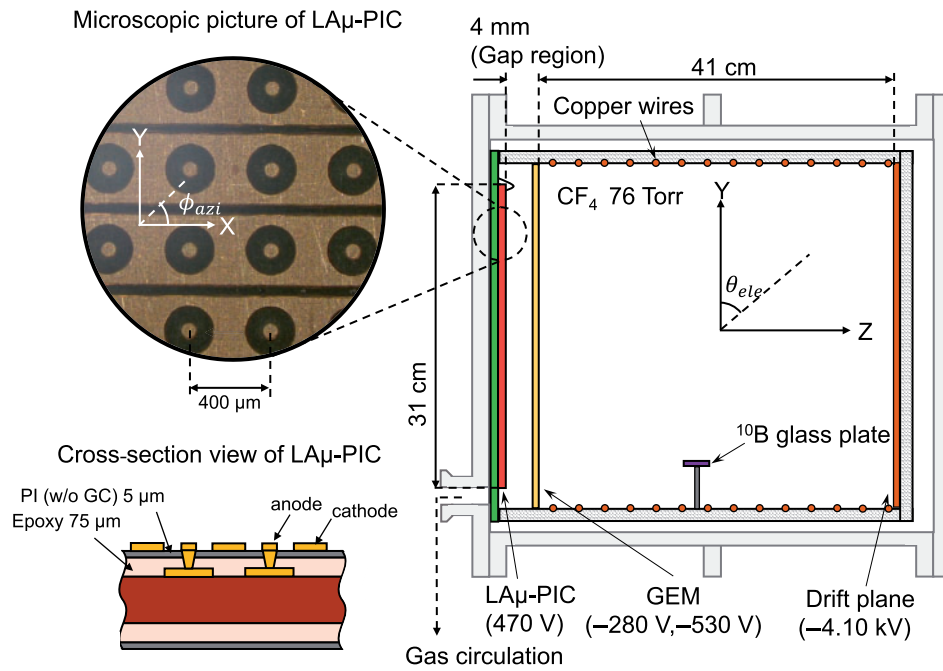


**Fig. 1.** Schematic drawings of the NEWAGE-0.3b'' detector. The top left-hand microscope picture shows the pixel electrode structure of the LA $\mu$ -PIC. The bottom left-hand drawing is the cross-section of the LA $\mu$ -PIC. The surface material is a combination of epoxy and polyimide without the glass cloth-sheet (GC). The NEWAGE-0.3b'' chamber is shown in the right-hand drawing. The LA $\mu$ -PIC has a detection area of  $31 \times 31$  cm<sup>2</sup> and the drift length is 41 cm. The gap region is defined as the volume between the LA $\mu$ -PIC and the GEM. The <sup>10</sup>B glass plate is set inside the TPC field cage for the energy calibration.

circulation system with a cooled charcoal (TSURUMICOAL 2GS) of 100 g was installed in order to remove radons.

The charge signals are read out from the anode and cathode electrodes with amplifier-shaper-discriminator chips (SONY CXA3653Q [23]). These signals are divided into digitized and analog signals. The digitized signals are sent to the FPGA-based encoding system and the hit-patterns are recorded with a clock of 100 MHz. In addition, the time-over-thresholds (TOTs) of each strip are recorded. The track length and direction are reconstructed using this information (see Ref. [18] for details). Analog signals of the 768 cathode strips are grouped into four channels and each channel is then divided into two. One of the divided signals is directly connected to a waveform digitizer (REPIC RPV160, 100 MHz), while the other is attenuated by a factor of three and read by the waveform digitizer. The waveforms are mainly used to determine the energy deposit of each event.

The energy calibration is performed with alpha-rays generated in a <sup>10</sup>B( $n, \alpha$ )<sup>7</sup>Li reaction. A glass plate with a thin <sup>10</sup>B layer is installed inside the  $\mu$ TPC. The detector is irradiated with neutrons from a <sup>252</sup>Cf fission source placed outside of the vessel and the neutrons are thermalized by polyethylene blocks. A continuous spectrum with a maximum edge at 1.5 MeV because of the thickness of the <sup>10</sup>B layer is obtained. The measured spectrum is fitted with simulated ones and the calibration factor converting the charge to energy is determined.

## 2.2. Performance

The following four analysis cuts were applied in order to select nuclear recoil events. Here the <sup>252</sup>Cf neutron calibration data was taken without polyethylene blocks in order to induce the fast neutron–nuclear scatterings.

- Fiducial cut: The fiducial area of the  $XY$  plane was defined as  $28 \times 24 \text{ cm}^2$ . The whole part of the track is required to be in the fiducial volume. This cut removes the charged particles from the wall and the  $^{10}\text{B}$  glass plate.
- Length–Energy cut: The stopping powers of nuclei are larger than those of electrons. Hence the track length vs. energy distribution can be used to identify the nuclear recoil tracks. Figure 2(a) shows the track length vs. energy distributions for the  $^{252}\text{Cf}$  calibration (black points) and the  $^{137}\text{Cs}$  calibration (blue points). From the  $^{252}\text{Cf}$  calibration data, we determined the nuclear band by fitting with a Gaussian function for every energy bin with a width of 10 keV. This cut removes electrons and alpha-rays.
- TOT–Energy cut: Energy deposition on a single strip is stored as TOT. Since nuclear recoil events have larger energy losses than electron events, the sum of TOT (TOT-sum) for a given energy tends to be large. In addition, since TOT-sum was expected to be linear with respect to the total energy deposit, a parameter defined by dividing the TOT-sum by energy was suitable for this purpose. Figure 3 (a) shows TOT-sum/energy vs. energy distributions for the  $^{252}\text{Cf}$  calibration (black points) and the  $^{137}\text{Cs}$  calibration (blue points). From the  $^{252}\text{Cf}$  calibration data, we determined the nuclear band by fitting every energy bin with a width of 10 keV with a Gaussian function. This cut rejects electron events.
- Roundness cut: The roundness is defined as a reduced chi-square value of a linear fit to the track. While the self-triggering mode TPC is not able to measure the absolute  $z$  position, this parameter is known to show some correlation with the absolute  $z$  position. For instance, small- $z$  events have short drift lengths, and thus the effect of electron diffusion is negligible. The track information keeps its original shape and is fitted well with a straight line. On the other hand, large- $z$  events are largely affected by electron diffusions, and the fitness to a straight line would be worse. In other words, these large- $z$  events have large roundness. Hence the roundness correlates with the absolute  $z$  position. Especially, this parameter is useful to remove “gap events”. The gap events are defined as events depositing all their energy in the gap region (Fig. 1). These gap events are not amplified by the GEM and thus the measured charge is smaller than those in the detection volume by a factor of the GEM gain. In order to reproduce the gap events, we irradiated the detector with neutrons from a  $^{252}\text{Cf}$  fission source without a drift electric field. Figure 4 (a) shows the roundness vs. energy distribution for the gap events. The roundness of gap events (red points) was found to be small. The events with roundness  $> 0.05$  are selected in order to remove gap events.

The nuclear detection efficiency was evaluated by irradiating the  $\mu\text{TPC}$  with neutrons from a  $^{252}\text{Cf}$  fission source. In order to cancel the  $x$ -,  $y$ - and  $z$ -position dependence of  $\mu\text{TPC}$  and evaluate overall efficiency, we needed homogeneous irradiation throughout the detection volume. We confirmed by Monte Carlo simulations that homogeneous irradiation in the TPC is made when  $^{252}\text{Cf}$  fission sources were set at six positions. In the actual measurement, we set a  $^{252}\text{Cf}$  source at one of the six positions and took the data, then moved the source to another position. We performed the measurements six times in series and combined the data in the analysis to realize homogeneous irradiation. The detection efficiency was calculated by comparing the measured energy and the simulated one. The measured detection efficiencies of the nuclear recoil events are shown in Fig. 5. The black and red lines are fitted lines of experimental data and indicate the detection efficiency when we applied only the fiducial cut and all event selections. The efficiency for all event selections was 14% at 50 keV.

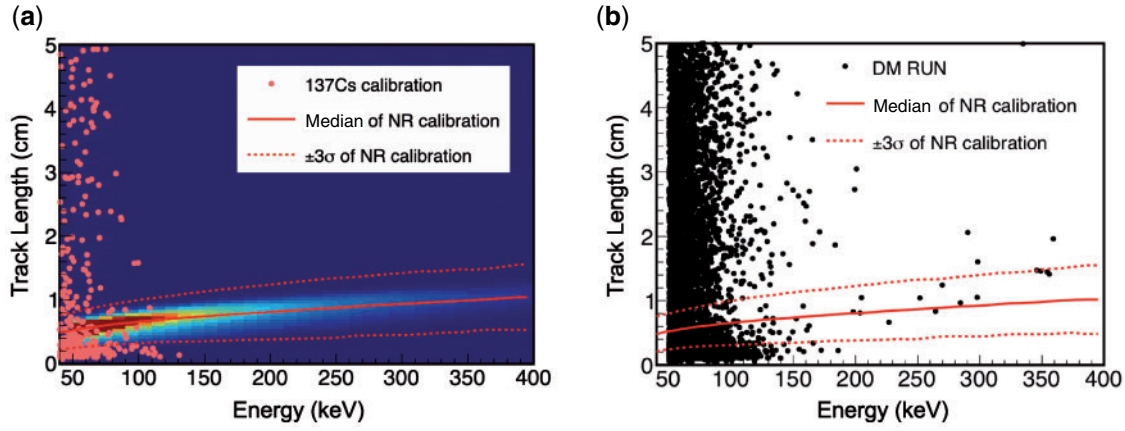


**Fig. 2.** Track-length vs. energy distributions. (a) The gradation and red dots represent the  $^{252}\text{Cf}$  neutron calibration data and the  $^{137}\text{Cs}$  electron calibration data, respectively. The solid and dotted red lines indicate the median and  $\pm 3\sigma$  quantiles of the neutron calibration, respectively. (b) Scientific RUN data (DM RUN) after the fiducial cut.

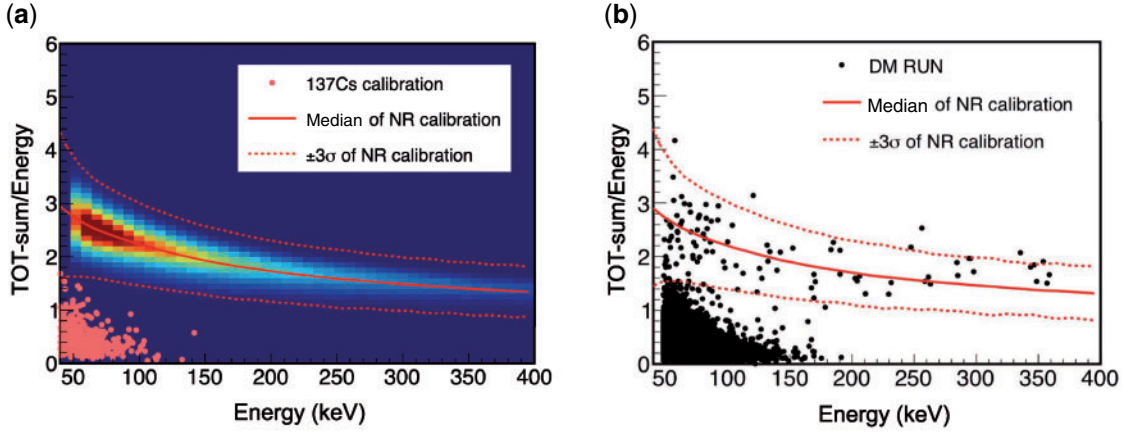


**Fig. 3.** TOT-sum/energy vs. energy distributions. (a) The gradation and red points represent the  $^{252}\text{Cf}$  neutron calibration data and the  $^{137}\text{Cs}$  electron calibration data, respectively. The solid and dotted red lines indicate the median and  $\pm 3\sigma$  quantiles of the neutron calibration, respectively. (b) Scientific RUN data (DM RUN) after the fiducial cut.

The  $\mu\text{TPC}$  has a non-isotropic response with regard to the nuclear recoil track direction because of the track-reconstruction algorithm. Thus, we need to measure the relative direction-dependent efficiency of nuclear recoil in the energy range of 50–100 keV. Figure 6 shows the measured distribution of the elevation angle  $\theta_{\text{ele}}$  and the azimuth angle  $\phi_{\text{azi}}$  in the detector coordinate. Although an ideal directional detector is expected to have a uniform distribution, our detector is not optimized yet in terms of the uniformity for the directional response. The efficiency is low around the  $XY$ ,  $XZ$  and  $YZ$  planes in any energy region because of the poor track reconstruction along anode/cathode strips. In addition, there are higher-efficiency areas along the diagonal lines from the direction of the anode and the cathode strips. This is because the current tracking algorithm tends to recognize the diffused tracks in such directions. We evaluated the gamma rejection power, or the detection efficiency of electrons, by irradiating the detector with gamma-rays from a  $^{137}\text{Cs}$  source. The gamma rejection power or the electron detection efficiency for the energy range of 50–60 keV was  $1.3^{+3.0}_{-1.1} \times 10^{-6}$ .



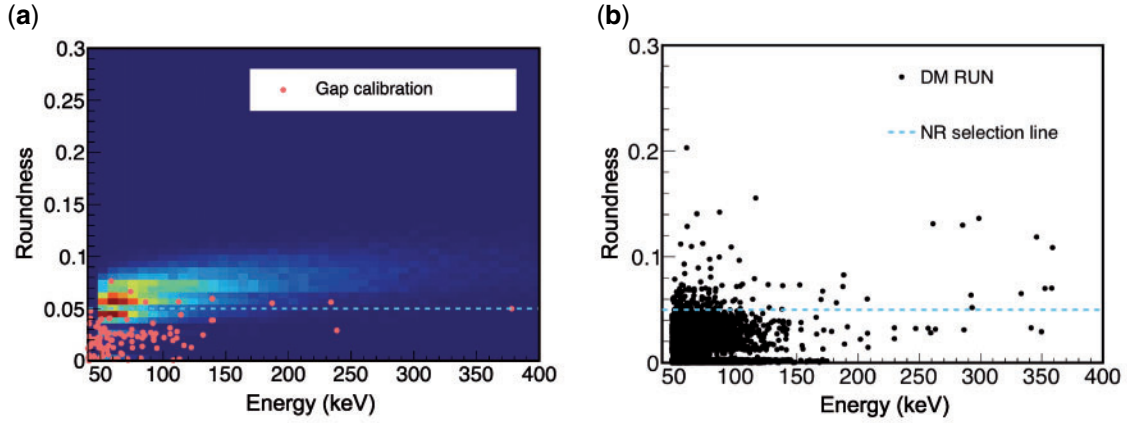


**Fig. 4.** Roundness vs. energy distribution. (a) The gradation and red points represent the  $^{252}\text{Cf}$  neutron calibration with a drift electric field and without a drift electric field, respectively. The dotted cyan line (roundness = 0.05) indicate the nuclear selection line. (b) Scientific RUN data (DM RUN) after the fiducial cut.

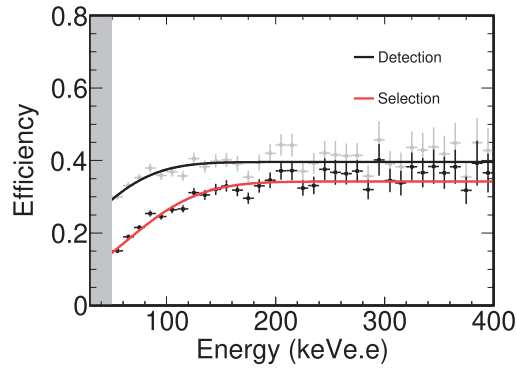


**Fig. 5.** Typical detection efficiency for nuclear recoil events. The gray and black points with errors are experimental data after the fiducial cut and the roundness cut, respectively. The solid black fitted line is the detection efficiency in the fiducial volume. The solid red fitted line is the detection efficiency after all event selections.

The angular resolution was evaluated using the neutron–nuclei elastic scatterings of the same method as in a previous study [24]. The angular  $\theta$  is defined as the angle between the direction of the scattered nuclei and the neutron source. We evaluated the angular resolution by the comparison of measured and simulated distributions of the recoil angle  $\cos \theta$ . The obtained angular resolution was  $48.0^{+6.8}_{-2.2}$  degrees in the energy range of 50–100 keV. The expected forward–backward ratio of  $|\cos \theta_{\text{cygnus}}|$  for the 100 GeV  $c^{-2}$  WIMP is 30%. Here  $\theta_{\text{cygnus}}$  is defined as the angle between the WIMP-wind direction and the measured direction of the recoil nucleus.

### 3. Experiment

A directional dark matter search (RUN22) was carried in Laboratory B of the Kamioka Observatory (36.25N, 137.18E) located at 2700 m water equivalent underground. The  $\text{LA}\mu\text{-PIC}$  plane was placed vertically and the  $z$ -axis is aligned to the direction of S30°E. The first sub RUN was performed from 2018 June 6 to August 24 and the second sub RUN was carried out from 2018 September 20 to November 14. The target gas is  $\text{CF}_4$  at 76 Torr (0.1 bar) and the target mass in the fiducial volume of  $28 \times 24 \times 41 \text{ cm}^3$  (28 L) is 10 g. The total live time is 107.6 d, corresponding to an exposure of 1.1 kg d.

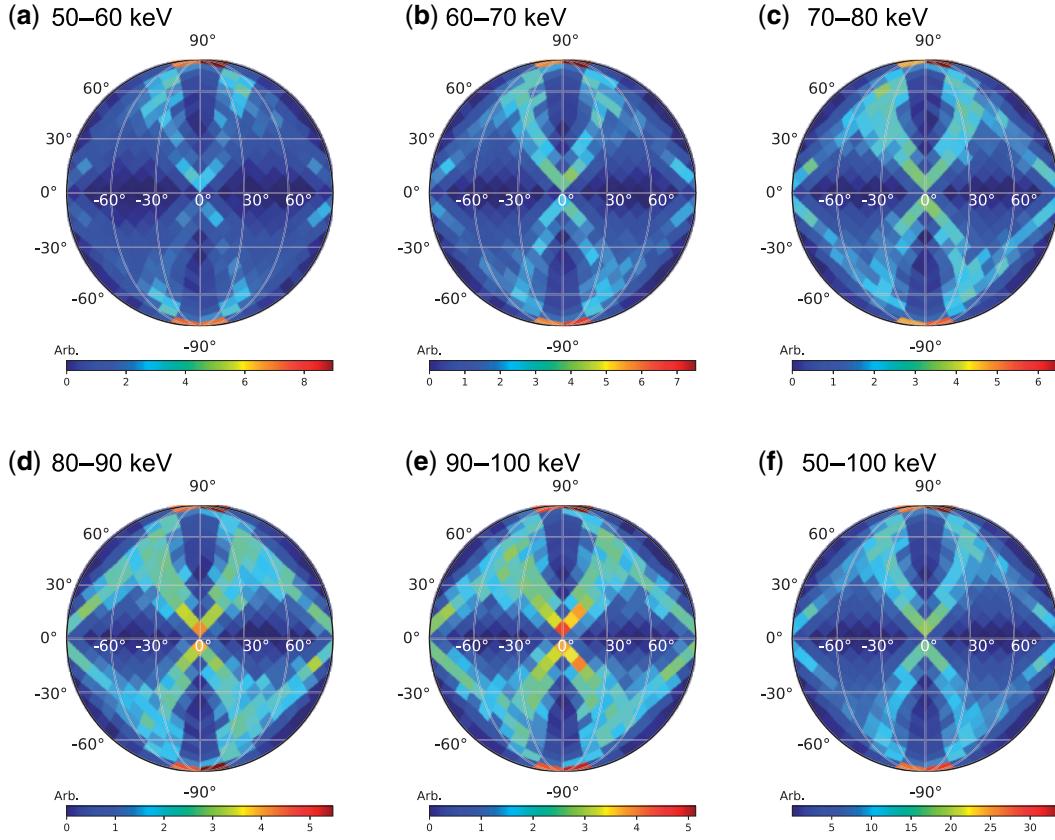


**Fig. 6.** Relative direction-dependent efficiencies in each energy region. The axes with white and black labels are the azimuth angle  $\phi_{\text{azi}}$  and the elevation angle  $\theta_{\text{ele}}$  in the detector coordinate, respectively. The  $x$ -axis and  $y$ -axis correspond to  $(\phi_{\text{azi}}, \theta_{\text{ele}}) = (0, 0)$  and  $(\phi_{\text{azi}}, \theta_{\text{ele}}) = (90, 0)$ , respectively.

The energy calibration and the detection efficiency measurement were carried out every two weeks. The gas gain at the beginnings of the sub RUNs was about 1100, and a time-dependent variation was observed due to the gas deterioration. The energy scale of the data was corrected considering the time-dependence of the gas gain. The energy resolution was  $13.2 \pm 2.3\%$  above 50 keV. The measured drift velocity at the beginnings of the sub RUNs was  $9.6 \text{ cm } \mu\text{s}^{-1}$  and the gas deterioration gave  $+3.3\%$  and  $-12\%$  of the maximum uncertainty.

The Length–Energy, TOT–Energy and Roundness–Energy distributions after the fiducial cut for the dark matter search data are shown in Figs. 2(b), 3(b) and 4(b), respectively. A large fraction of the events has long track lengths and small TOTs, which indicates that most of the measured events are electrons. These events are effectively reduced by analysis cuts introduced in Sec. 2.2. Energy spectra at each cut stage are shown in Fig. 7(a). The final event sample was reduced to 17 events in the energy region of 50–400 keV owing to analysis cuts using track information without any shields such as Pb. Since the directionality is lost in the energy below 50 keV because of the short tracks and the diffusion effect, the lower energy bound is set at 50 keV. The energy spectrum for the final sample unfolded by the nuclear detection efficiency is shown in Fig. 7(b) together with one of the previous results of RUN14 [17] using the standard  $\mu$ -PIC. The main background of RUN14 in 50–100 keV are alpha-rays radiated from the surface material of the standard  $\mu$ -PIC. These backgrounds were reduced in RUN22 by about a factor of 10 thanks to the LA $\mu$ -PIC, the surface material of which is

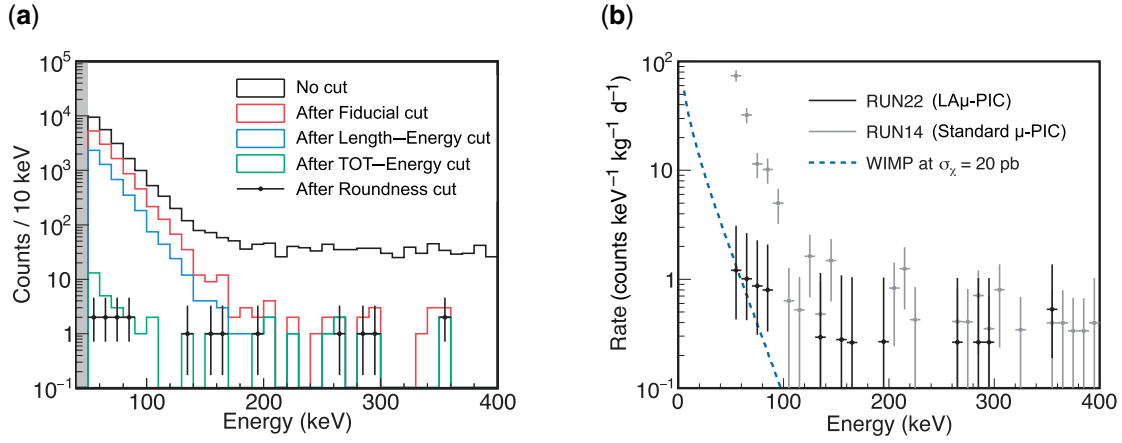


**Fig. 7.** (a) Energy spectra of the dark matter search at each selection step. The black, red, blue and green lines are the no-cut energy spectrum, and those after the Fiducial cut, the Length–Energy cut and the TOT–Energy cut, respectively. The black points with error bars are the final event sample after the Roundness cut. (b) Final energy spectrum considering the detection efficiency. The black and gray points with error bars represent RUN22 (using the LA $\mu$ -PIC) and RUN14 (using the standard  $\mu$ -PIC), respectively. Error bars indicate statistic poisson errors. The dotted blue line shows the expected spectrum of the WIMP-nucleus scattering with the WIMP mass of 100 GeV  $c^{-2}$ , the WIMP-proton cross-section of  $\sigma_{\chi} = 20$  pb and the energy resolution of 13.2%.

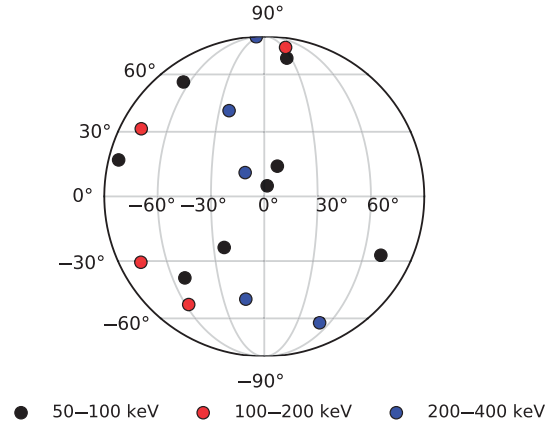


**Fig. 8.** Skymap of the final sample on the detector coordinate. The black, red and blue points show the energy regions of 50–100 keV, 100–200 keV and 200–400 keV, respectively.

less contaminated with  $^{238}\text{U}$  and  $^{232}\text{Th}$ . It is demonstrated that the LA $\mu$ -PIC works as expected to reduce the alpha-ray backgrounds.

Figure 8 shows the skymap of the final sample on the detector coordinate. We calculated the nuclear recoil distribution  $|\cos \theta_{\text{cygnus}}|$  for the energy region of 50–100 keV in order to evaluate the forward–backward asymmetry. Figure 9 shows the measured and expected  $|\cos \theta_{\text{cygnus}}|$  distribution binned into two for each energy range. As a model-independent interpretation of these results, we first set upper limits on the forward–backward asymmetry parameters based on the raw counting numbers in each energy bin. The forward–backward asymmetry parameter is defined as the ratio of the first and second bins. The 90% confidence level upper limits of these values in 50–60 keV, 60–70 keV, 70–80 keV and 80–90 keV are 2.3, 3.9, 5.3 and 3.9, respectively. The systematic uncertainties of the expected rate for the WIMP were summarized in Table 1. The angular resolution gives the dominant



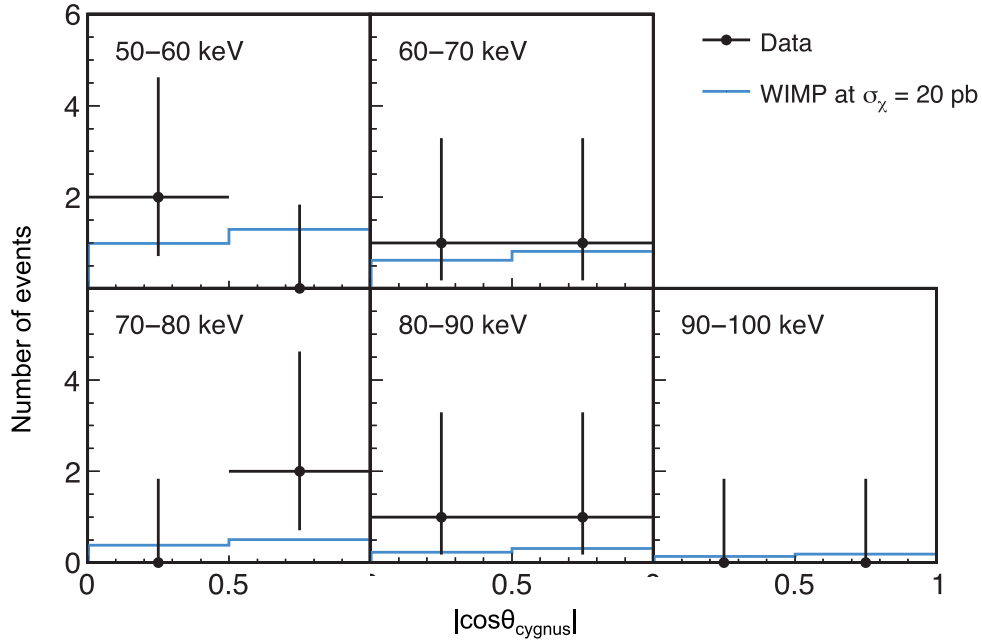


**Fig. 9.** Measured and expected  $|\cos\theta_{\text{cygnus}}|$  distribution for each energy range. The black points with errors are measured data. The cyan lines show the WIMP expected signal of the WIMP-nucleus scattering with the WIMP mass of  $100 \text{ GeV } c^{-2}$  and the WIMP-proton cross-section of  $\sigma_{\chi} = 20 \text{ pb}$ .

**Table 1.** Systematic uncertainties of the expected rate for the WIMP mass  $m_{\chi} = 100 \text{ GeV } c^{-2}$ .

Source	$\cos\theta$ range	Relative uncertainty (%)
Energy resolution	[ 0, 1 ]	< 0.1
Drift velocity	[ 0, 0.5 ]	< 0.2
	[ 0.5, 1 ]	< 0.2
Angular resolution	[ 0, 0.5 ]	+5.4 –2.2
	[ 0.5, 1 ]	+1.7 –4.2

systematic uncertainty, which impacts the shape of the nuclear recoil distribution, and is considered in the following statistic test.

#### 4. Results

In order to obtain a possible anisotropic  $|\cos\theta_{\text{cygnus}}|$  distribution, a binned likelihood-ratio method was used [25]. The minimized statistic value  $\chi^2$  was defined as,

$$\chi^2 = 2 \sum_{i=0}^n \left[ (N_i^{\text{exp}} - N_i^{\text{data}}) + N_i^{\text{data}} \ln \left( \frac{N_i^{\text{data}}}{N_i^{\text{exp}}} \right) \right] + \alpha^2, \quad (1)$$

where the subscript  $i$  is the bin number of  $|\cos\theta_{\text{cygnus}}|$  distribution,  $N_i^{\text{data}}$  is the measured number of events and  $N_i^{\text{exp}}$  is the expected number of events. A nuisance parameter  $\alpha (= \xi/\sigma_{\kappa})$  was introduced to consider the systematic uncertainty of the angular resolution  $\sigma_{\kappa}$ . A possible angular-resolution shift is  $\xi$ . The expected event number  $N_i^{\text{exp}}$  was obtained by a signal Monte Carlo simulation. It depends on the WIMP mass  $m_{\chi}$ , the WIMP-proton cross-section  $\sigma_{\chi-p}$  and the astrophysical parameters. In

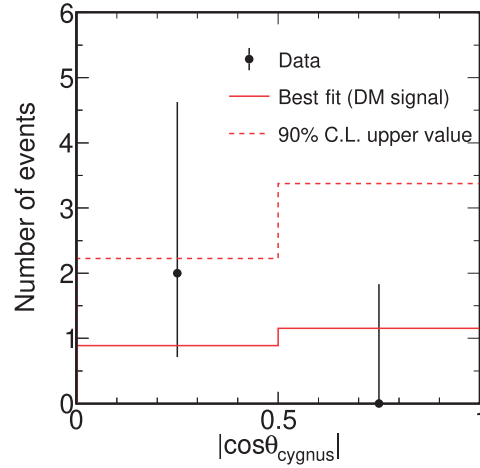


**Fig. 10.** The  $|\cos \theta_{\text{cygnus}}|$  distribution in the energy range of 50–60 keV. The black points show observed data. The solid and dotted red lines are the simulated distribution using best-fitting values and excluded values of 90% C.L., respectively.

addition, the nuclear quenching factor and the detector responses were considered. Here the nuclear quenching factor was simulated by SRIM [26], which represented the experimental alpha-ray data of the previous experiment [27]. The energy bin was divided into 10 keV per bin considering the energy resolution. Since each energy bin had low statistics, the measured  $|\cos \theta_{\text{cygnus}}|$  were binned into two.

The measurement data was fitted by minimizing  $\chi^2$  using an anisotropic WIMP model. Here, no background (BG) was added in order to prevent any uncertainty of the BG distribution. The WIMP-proton cross-section  $\sigma_{\chi-p}$  and the nuisance parameter  $\alpha$  were treated as fitting parameters. The minimum  $\chi^2$  value for the 50–60 keV bin was 3.3, where  $\sigma_{\chi-p}$  and  $\alpha$  were 18.5 pb and 0.12, respectively. Figure 10 shows the measured  $|\cos \theta_{\text{cygnus}}|$  distribution in the energy region of 50–60 keV along with the expected one using best-fitting values. In order to calculate the p-value, we made a  $\chi^2$  distribution of an isotropic BG model and an anisotropic WIMP model from dummy samples. One thousand dummy samples were produced by Monte Carlo simulations and the  $\chi^2$  value of each dummy sample was calculated. P-values for both the WIMP and BG model were 3.3%. Hence we cannot claim the detection of WIMP dark matter with sufficient significance from the observed data. This is a natural result because of the large statistic error and the small expected anisotropic ratio. Since no significant amplitude was found, a 90% confidence level (C.L.) upper limit was set on the SD cross-section. The 90% C.L. upper limit on the SD cross-section was obtained as 50 pb for 100-GeV WIMPs. Figure 11 shows the 90% C.L. upper limit on the SD WIMP-proton cross-section as a function of the WIMP mass. This result marked a new best sensitivity record in the SD WIMP search with the direction-sensitive method. This result improved the constraint by about 15 times compared to the previous result of RUN14-18. This improvement is owing to the surface background reduction of the  $\mu$ -PIC detector.

## 5. Discussion

One of the milestones of the NEWAGE is to search an allowed region from the DAMA experiment [30] with the directional method. An improvement of more than two orders of magnitude is

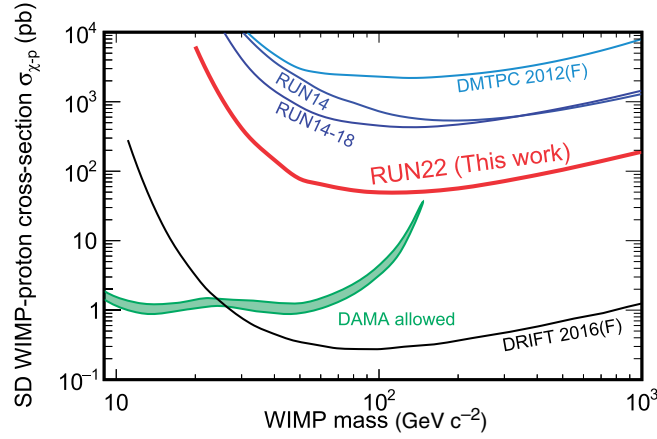


**Fig. 11.** 90% C.L. upper limits on the SD WIMP-proton cross-section as a function of the WIMP mass. The thick solid red line is the result of the directional method in this work. The solid blue lines of RUN14 and RUN14-18 are our previous results [17,18]. The solid light-blue and black lines show the results from the directional analysis of DMTPC [28] and the conventional analysis without the directional sensitivity of DRIFT [29], respectively. The allowed region from DAMA/LIBRA experiment [30] is shown by the green area.

required in order to cover the entire DAMA region. Since the sensitivity is limited by the remaining backgrounds, we investigated the origin of these backgrounds in RUN22 using a Geant4 [31] simulation.

The main internal background candidates are alpha-rays coming from the decay of radons and the  $\text{LA}\mu\text{-PIC}$  surface. The alpha-rays cannot be discriminated from nuclear recoil events around 50 keV in the NEWAGE-0.3b'' detector by analysis cuts. Hence screening the material of the TPC and the  $\text{LA}\mu\text{-PIC}$  is needed. A broad peak is observed in the energy spectrum around 6 MeV corresponding to the  $^{220}\text{Rn}$  and  $^{222}\text{Rn}$  decay during the dark matter search [32]. The estimated contamination of  $^{220}\text{Rn}$  and  $^{222}\text{Rn}$  is  $5.7 \pm 0.3 \text{ mBq m}^{-3}$  and  $(5.3 \pm 2.1) \times 10^{-1} \text{ mBq m}^{-3}$ , respectively. In the Geant4 simulation, we generated alpha-rays from decay chains of  $^{220}\text{Rn}$  and  $^{222}\text{Rn}$  inside the TPC according to the branching ratio and estimated the number of events, or the rate, with the analysis cut in the same way as RUN22. The expected number of events (rate) due to  $^{220}\text{Rn}$  and  $^{222}\text{Rn}$  contamination in the low-energy region of 50–60 keV were  $(6.1 \pm 0.7) \times 10^{-1}$  ( $5.5 \times 10^{-2} \text{ dru}^1$ ) and  $(5.3 \pm 2.2) \times 10^{-2}$  ( $4.7 \times 10^{-3} \text{ dru}$ ), respectively. The remaining alpha-ray emission rate of the  $\text{LA}\mu\text{-PIC}$  was  $(2.1 \pm 0.5) \times 10^{-4} \text{ alpha cm}^{-2} \text{ hr}^{-1}$  [21] and the dominant component were 5.3-MeV alpha-rays from  $^{210}\text{Po}$  decay. The expected number of events (rate) in the 50–60 keV region from this background was less than  $1.2 \times 10^{-1}$  ( $1.1 \times 10^{-2} \text{ dru}$ ).

Ambient gamma-rays and neutrons from rocks in the mine are two of the main components of the external background. Contributions of the cosmic-ray muons are negligible compared with ambient gamma-rays and neutrons. Measured ambient gamma-ray flux in the Laboratory B [33] was used for the estimation. The expected counts (rate) in the energy range of 50–60 keV was  $1.5 \pm 1.5$  ( $1.4 \times 10^{-1} \text{ dru}$ ). The ambient neutron flux was measured using a  $^3\text{He}$  proportional counter and an energy spectrum of ambient neutrons produced by  $(\alpha, n)$  reactions and spontaneous fission was predicted [34]. The expected counts (rate) in the energy range of 50–60 keV is  $(3.5 \pm 0.9) \times 10^{-1}$  ( $3.1 \times 10^{-2} \text{ dru}$ ). The expected number of background events in the energy region of 50–60 keV

<sup>1</sup> dru=counts/sec/keV/kg

**Table 2.** Summary of the expected numbers of background events and measured numbers in the energy region of 50–60 keV.

Source	w/ Roundness	w/o Roundness
Ambient gamma-rays	$1.5 \pm 1.5$	$4.6 \pm 2.7$
Ambient neutrons	$(3.5 \pm 0.9) \times 10^{-1}$	$(4.8 \pm 1.2) \times 10^{-1}$
$^{222}\text{Rn}$	$(5.3 \pm 2.2) \times 10^{-2}$	$(8.6 \pm 3.5) \times 10^{-2}$
$^{220}\text{Rn}$	$(6.1 \pm 0.7) \times 10^{-1}$	$1.1 \pm 0.1$
LA $\mu$ -PIC surface	$< 1.2 \times 10^{-1}$	$9.1 \pm 2.3$
Total background	$2.5 \pm 1.5$	$15 \pm 3.5$
Measurement	$2.0 \pm 1.4$	$12 \pm 3.5$

is summarized in Table 2. The result without a roundness-cut is also shown in order to confirm the alpha-ray backgrounds from the LA $\mu$ -PIC surface directly. The measured number of events are in good agreement with what is predicted, within errors, for both with and without the roundness-cut.

The  $^{222}\text{Rn}$  backgrounds were reduced by the gas circulation system with cooled charcoal and their contribution was found to be negligible. Ambient gamma-rays and ambient neutrons contribute some part of the backgrounds. These backgrounds can be reduced by the external shields comprising materials like lead (Pb) and water (H<sub>2</sub>O). On the other hand, internal backgrounds of  $^{220}\text{Rn}$  and the LA $\mu$ -PIC surface would remain with the external shields and they would be dominant backgrounds. A straightforward way of reducing these backgrounds is to replace the detector components with radiopure materials. A  $\mu$ -PIC with a further background reduction is being developed. Another approach to reduce the background is to detect the absolute  $z$  position of the events. The majority of the remaining backgrounds are known to be located at low  $z$  (around the LA $\mu$ -PIC and the GEM) and high- $z$  position (around the drift plate). A discovery of minority carriers in CS<sub>2</sub> + O<sub>2</sub> gas mixtures by the DRIFT group opened the potential of an absolute  $z$  measurement in self-triggering TPCs [29]. We have recently demonstrated a 3D tracking with a spatial resolution of 130  $\mu\text{m}$  using the  $\mu$ -PIC in a negative ion gas SF<sub>6</sub>. Simultaneously, the absolute  $z$  coordinate was determined with a location accuracy of 16 mm [35]. The negative ion gas TPC enables us to reduce these backgrounds using the  $z$  fiducialization, effectively. Thus the use of the negative ion gas TPC is another promising approach to reduce the surface alpha-ray backgrounds. It should be noted that the surface background will be one of the ultimate background sources even after significant efforts of material selection since radioactive isotopes can be embedded by the decays of radons in a normal atmosphere even after the production. Thus it is important to take both possible ways to reduce the background so as to start investigating the DAMA region and further searches.

## 6. Conclusion

We developed a low-background  $\mu$ TPC detector, NEWAGE-0.3b”, for the directional dark matter search with an LA $\mu$ -PIC, which is a 2D tracking gaseous detector made of low-radioactive materials. A directional dark matter search in the Kamioka Observatory was carried out in 2018. The total exposure was 1.1 kg d and the number of the observed events in the energy region of 50–60 keV was two, which is consistent with the expected number of background events of 2.5. No significant forward–backward asymmetry of a WIMP signal was found, therefore we derived a 90% confidence level upper limit on the SD WIMP-proton cross-section of 50 pb for 100 GeV  $c^{-2}$  WIMPs. We improved the constraint of the previous result [17] by a factor of 15 and marked the best direction-sensitive limit.

## Acknowledgements

This work was partly supported by Japan Society for the promotion of Science (JSPS) KAKENHI (Grant-in-Aids for Scientific Research) (grant nos. 16H02189, 19684005, 23684014 and 26104005, 19H05806), JSPS Bilateral Collaborations (Joint Research Projects and Seminars) program, ICRR Joint-Usage, Program for Advancing Strategic International Networks to Accelerate the Circulation of Talented Researchers (R2607), and JSPS Research Fellow (grant nos. 17J03537).

## Funding

Open Access funding: SCOAP<sup>3</sup>.

## References

- [1] E. Aprile et al. [XENON Collaboration], Phys. Rev. Lett. **121**, 111302 (2018).
- [2] D. S. Akerib et al. [LUX Collaboration], Phys. Rev. Lett. **118**, 021303 (2017).
- [3] R. Agnese et al., Phys. Rev. Lett. **121**, 051301 (2018); **122**, 069901 (2019) [erratum].
- [4] P. Agnes et al. [DarkSide Collaboration], Phys. Rev. Lett. **121**, 081307 (2018).
- [5] R. Ajaj et al. [DEAP Collaboration], Phys. Rev. D **100**, 022004 (2019).
- [6] E. Armengaud et al., J. Cosmol. Astropart. Phys. **1605**, 019 (2016).
- [7] X. Cui et al. [PandaX-II Collaboration], Phys. Rev. Lett. **119**, 181302 (2017).
- [8] K. Abe et al. [XMASS Collaboration], Phys. Lett. B **759**, 272 (2016).
- [9] S. Baum, K. Freese, and C. Kelso, Phys. Lett. B **789**, 262 (2019).
- [10] D. N. Spergel, Phys. Rev. D **37**, 1353 (1988).
- [11] C. A. J. O'Hare, A. M. Green, J. Billard, E. Figueroa-Feliciano, and L. E. Strigari, Phys. Rev. D **92**, 063518 (2015).
- [12] J. Billard, F. Mayet, and D. Santos, Phys. Rev. D **83**, 075002 (2011).
- [13] S. K. Lee and A. H. G. Peter, J. Cosmol. Astropart. Phys. **1204**, 029 (2012).
- [14] K. I. Nagao, T. Ikeda, R. Yakabe, T. Naka, and K. Miuchi, Phys. Dark Univ. **27**, 100426 (2020).
- [15] K. Miuchi, H. Kubo, T. Nagayoshi, A. Ochi, R. Orito, A. Takada, T. Tanimori, and M. Ueno, IEEE Trans. Nucl. Sci. **50**, 825 (2003).
- [16] A. Takada et al., Nucl. Instrum. Methods Phys. Res. A **573**, 195 (2007).
- [17] K. Nakamura et al., Prog. Theor. Exp. Phys. **2015**, 043F01 (2015).
- [18] R. Yakabe et al., Prog. Theor. Exp. Phys. **2020**, 113F01 (2020).
- [19] T. Hashimoto, K. Miuchi, K. Nakamura, R. Yakabe, T. Ikeda, R. Taishaku, M. Nakazawa, H. Ishiura, A. Ochi, and Y. Takeuchi, AIP Conf. Proc. **1921**, 070001 (2018).
- [20] F. Sauli, Nucl. Instrum. Methods Phys. Res. A **805**, 2 (2016).
- [21] T. Hashimoto et al., Nucl. Instrum. Methods Phys. Res. A **977**, 164285 (2020).
- [22] T. Tamagawa et al., Nucl. Instrum. Methods Phys. Res. A **608**, 390 (2009).
- [23] R. Orito, O. Sasaki, H. Kubo, K. Miuchi, T. Nagayoshi, Y. Okada, A. Takada, A. Takeda, T. Tanimori, and M. Ueno, IEEE Trans. Nucl. Sci. **51**, 1337 (2004).
- [24] K. Nakamura et al., J. Instrum. **7**, C02023 (2012).
- [25] J. Conrad, O. Botner, A. Hallgren, and C. Pérez de los Heros, Phys. Rev. D **67**, 012002 (2003).
- [26] J. F. Ziegler, M. D. Ziegler, and J. P. Biersack, Nucl. Instrum. Methods Phys. Res. B **268**, 1818 (2010).
- [27] H. Nishimura et al., Astropart. Phys. **31**, 185 (2009).
- [28] S. Ahlen et al. [DMTPC Collaboration], Phys. Lett. B **695**, 124 (2011).
- [29] J. B. R. Battat et al., Phys. Dark Univ. **9–10**, 1 (2015).
- [30] C. Savage, P. Gondolo, and K. Freese, Phys. Rev. D **70**, 123513 (2004).
- [31] S. Agostinelli et al., Nucl. Instrum. Methods Phys. Res. A **506**, 250 (2003).
- [32] T. Ikeda, PhD thesis, Kobe University (2020).
- [33] H. Nishimura, PhD thesis, Kyoto University (2008).
- [34] K. Mizukoshi et al., Prog. Theor. Exp. Phys. **2018**, 123C01 (2018).
- [35] T. Ikeda, T. Shimada, H. Ishiura, K. D. Nakamura, T. Nakamura, and K. Miuchi, J. Instrum. **15**, P07015 (2020).